Author/s:
Ghasemian, MB;Zavabeti, A;Mousavi, M;Murdoch, BJ;Christofferson, AJ;Meftahi, N;Tang, J;Han, J;Jalili, R;Allioux, FM;Mayyas, M;Chen, Z;Elbourne, A;McConville, CF;Russo, SP;Ringer, S;Kalantar-Zadeh, K

Title:
Doping Process of 2D Materials Based on the Selective Migration of Dopants to the Interface of Liquid Metals

Date:
2021-10-01

Citation:
Ghasemian, M. B., Zavabeti, A., Mousavi, M., Murdoch, B. J., Christofferson, A. J., Meftahi, N., Tang, J., Han, J., Jalili, R., Allioux, F. M., Mayyas, M., Chen, Z., Elbourne, A., McConville, C. F., Russo, S. P., Ringer, S. & Kalantar-Zadeh, K. (2021). Doping Process of 2D Materials Based on the Selective Migration of Dopants to the Interface of Liquid Metals. Advanced Materials, 33 (43), https://doi.org/10.1002/adma.202104793.

Doping Process of Two-Dimensional Materials Based on the Selective Migration of Dopants to the Interface of Liquid Metals

Mohammad B. Ghasemian, Ali Zavabeti, Maedehsadat Mousavi, Billy J. Murdoch, Andrew J. Christofferson, Nastaran Meftahi, Jianbo Tang, Jialuo Han, Rouhollah Jalili, Francois-Marie Allioux, Mohannad Mayyas, Zibin Chen, Aaron Elbourne, Chris F. McConville, Salvy P. Russo, Simon Ringer, and Kourosh Kalantar-Zadeh**

Dr. M. B. Ghasemian, M. Mousavi, Dr. J. Tang, J. Han, Dr. R. Jalili, Dr. F.-M. Allioux, Dr. M. Mayyas and Prof. K. Kalantar-Zadeh

School of Chemical Engineering, University of New South Wales (UNSW), Sydney, New South Wales, Australia
E-mail: m.ghasemian@unsw.edu.au and k.kalantar-zadeh@unsw.edu.au

Dr. A. Zavabeti, Dr. A. J. Christofferson, Dr. Aaron Elbourne and Prof. C. F. McConville
School of Science, RMIT University, Melbourne, Victoria 3001, Australia

Dr. A. Zavabeti
Department of Chemical Engineering, The University of Melbourne, Parkville, Victoria, Australia

Dr. B. J. Murdoch

RMIT Microscopy and Microanalysis Facility, STEM College, RMIT University, Melbourne, Victoria 3001, Australia

This is the author manuscript accepted for publication and has undergone full peer review but has not been through the copyediting, typesetting, pagination and proofreading process, which may lead to differences between this version and the Version of Record. Please cite this article as doi: 10.1002/adma.202104793.

Dr. N. Meftahi and Prof. S. P. Russo
ARC Centre of Excellence in Exciton Science, School of Science, RMIT University, Melbourne, Victoria, Australia

Dr. Z. Chen and Prof. S. Ringer
School of Aerospace, Mechanical and Mechatronic Engineering, The University of Sydney, Sydney, NSW 2006, Australia

Prof. C. F. McConville

Institute for Frontier Materials, Deakin University, Geelong, Victoria 3216, Australia

Prof. S. Ringer
Australian Centre for Microscopy and Microanalysis, The University of Sydney, Sydney, NSW 2006, Australia

Keywords: Liquid metal, Atomically thin, Doping, Tin, Bismuth

The introduction of trace impurities within the doping processes of semiconductors is still a technological challenge for the electronics industries. By taking advantage of the selective enrichment of liquid metal interfaces, and harvesting the doped metal oxide semiconductor layers, the complexity of the process can be mitigated and a high degree of control over the outcomes can be achieved. Here we propose a mechanism of natural filtering for the preparation of doped two-dimensional (2D) semiconducting sheets based on the different migration tendencies of metallic elements in the bulk competing for enriching the interfaces. As a model, liquid metal alloys with different weight ratios of Sn and Bi in the bulk were employed for harvesting Bi_2O_3-doped SnO nanosheets. In this model, Sn shows a much stronger tendency than Bi to occupy surface sites of the

Bi-Sn alloys, even at the very high concentrations of Bi in the bulk. This provides the opportunity for creating SnO 2D sheets with tightly controlled Bi_2O_3 dopants. By way of example, we demonstrated how such nanosheets could be made selective to both reducing and oxidizing environmental gases. The process demonstrated here offers significant opportunities for future synthesis and fabrication processes in the electronics industries.

1. Introduction

Conventionally, the synthesis and fabrication processes used to process and manufacture electronic and optical devices are carried out in extremely clean environments under stringently controlled conditions. In the electronics industries, for the majority of synthesis and fabrication processes, the semiconductor structures used are fabricated to be ultra-pure materials. The smallest impurities in the process, either in the equipment or the atmosphere, can lead to a significant loss of functionality or deterioration of quality in the final device performance. Additionally, doping is generally an important part of the process. Dopants are introduced in strictly controlled amounts, especially when the dopants are added, as is usual, at low concentrations. The presence of impurities during the multi step doping process competes with the dopant atoms to alter the final characteristics of the materials. This challenge has been mitigated using high grade cleanrooms, complex instrumentation, and precise optimization of elemental stoichiometry. However, the current processes are both costly and complicated. Therefore, introducing efficient filtering methods, at low costs, to introduce dopants at the desired concentrations and avoid impurities is of great value. Liquid metal based processes offer a practical solution in this regard.[1-13]

In a liquid metal alloy, individual elements naturally compete to appear on the surface [14] and this likely offers a very efficient filter at the elemental level. Zavabeti *et al*.[14] have shown that even very small amounts of elements such as Al, Gd and Hf, added to the bulk of liquid metal such as Ga, can dominate the surface in the liquid state.[15] Following exposure of the surface to the ambient oxygen, 2D oxides of these additional elements dominate the interfacial region and appear uniformly above the Ga droplet on the surface. This occurs despite their remarkably low concentration in the bulk (>1 wt%). However, this filtering property can also be distorted by the characteristics of the alloying elements, and instead mixed oxides can appear on the surface of the liquid metal. For instance, a mixture of indium and tin was found on the surface after harvesting 2D indium tin oxide (ITO) sheets. However, even in this case, the elemental ratios at the surface differ significantly from the initial ratios of Sn and In incorporated in the bulk. Tin atoms showed a higher tendency to migrate to the surface compared to In atoms.[16] Altogether, while the surface oxide filters out the impurities, and more importantly the surface can be doped, the stoichiometry of the oxide layer can be controlled selectively even when the secondary material is added to the bulk at a high concentration.

Doped 2D semiconducting metal oxides are of particular interest where new guest species are inserted into the monolayer structures and, as the result, the original physical and chemical characteristics are altered, offering new properties and applications in electronics, optics, sensing, piezotronics, magnetism and catalysis.[17-23] Among 2D semiconducting metal oxides, tin monoxide (SnO) is known to be a high-performance wide band gap semiconductor showing intrinsic p-type

conductance. As one of the most promising oxides for next-generation transparent electronics and displays, SnO can also be doped with other materials to show both p- and n-type behaviour.[24] Large wafer-scale SnO monolayers have been shown to be produced using liquid metal exfoliation.[25] The surface of the molten tin is dominated by SnO due to the specific redistribution of Sn and O atoms across the interface, however, SnO_2 is also produced on the surface if the molten tin is exposed to high concentrations of oxygen for an extended period.[25]

The melting point of Sn is 231.9 °C, and it forms a eutectic alloy with a melting point of ~139 °C when combined with Bi at 43 wt% Sn and 57 wt% Bi.[26] Alloys with varying ratios of Bi and Sn (Bi-Sn alloys) can also be created with a range of melting points, some smaller than the melting points of both elements (melting point of Bi is 271.4 °C). A comparison of the Gibbs free energy (ΔG_f) for the formation of bismuth oxide and SnO,[14, 26] shows that when the surface of the Bi-Sn melts are exposed to a controlled amount of O_2, SnO always selectively forms on the surface. However, here we hypothesize that at high concentrations of Bi in the bulk, trace amounts of Bi can also migrate to the surface, doping the established 2D SnO nanosheets. We also predict that this will allow us to controllably change the doping concentration by altering the Bi volume in the bulk. Advantageously, this all occurs within the same process and hence reduces the need for a multi-step doping process. Another advantage is that the process takes place at very low temperatures. Generally, multi-step doping requires high temperature annealing as a step in the process or synthesized materials that inevitably introduce complexities and limitations to the fabrication of devices.

In this work, a one-step low-temperature printing technique has been employed to demonstrate the formation of delaminated large 2D SnO doped with Bi_2O_3 from the surface of liquid metal melt via a van der Waals printing process. Liquid metals serve as natural filtering to accommodate the target doping elements in the surface oxide layer. To achieve this, different alloys of Bi and Sn were prepared and the elemental dopant variations in the 2D structures were explored against the ratios of Bi and Sn in the bulk liquid metal alloys. Very high concentrations of metallic Bi were used while the diffusion of Bi as dopant from the bulk to surficial SnO was limited. The mechanism that describes the selective diffusion of Bi to the surface of the 2D films has been investigated both experimentally and using molecular dynamics (MD) simulations. Eventually, selective gas sensing is shown as a model application for highly controlled doping.

2. Results and Discussion

The schematic in **Figure 1a** illustrates the preparation of ultra-thin sheets which includes van der Waals exfoliation and printing from the surface of liquid metal to a substrate. In order to prepare ultra-thin layers of Bi-Sn materials, different weight ratios of Bi and Sn metals (0%, 20%, 40%, 57%, 80%, 90%, 100%) were mixed and melted together to produce Bi-Sn alloys of 100%Sn, 20%Bi, 40%Bi, 57%Bi, 80%Bi, 90%Bi, and 100%Bi. These alloys were melted at 300°C in an N_2 glove box with a limited level of oxygen (0.2% O_2) to control the interfacial oxidation. An atomically thin oxide layer emerges on the surface of the liquid metal through a self-limiting reaction (the Cabrera-Mott process) when the pristine molten metal droplet is exposed to ambient atmospheric

conditions. Although molten Sn, Bi and their alloys are in the liquid state, in ambient conditions the surfaces of these liquid metals are covered by tin and bismuth oxide atomically thin sheets (nanosheets), respectively, that are formed as a result of the interaction between the surficial layer of liquid metals and oxygen.

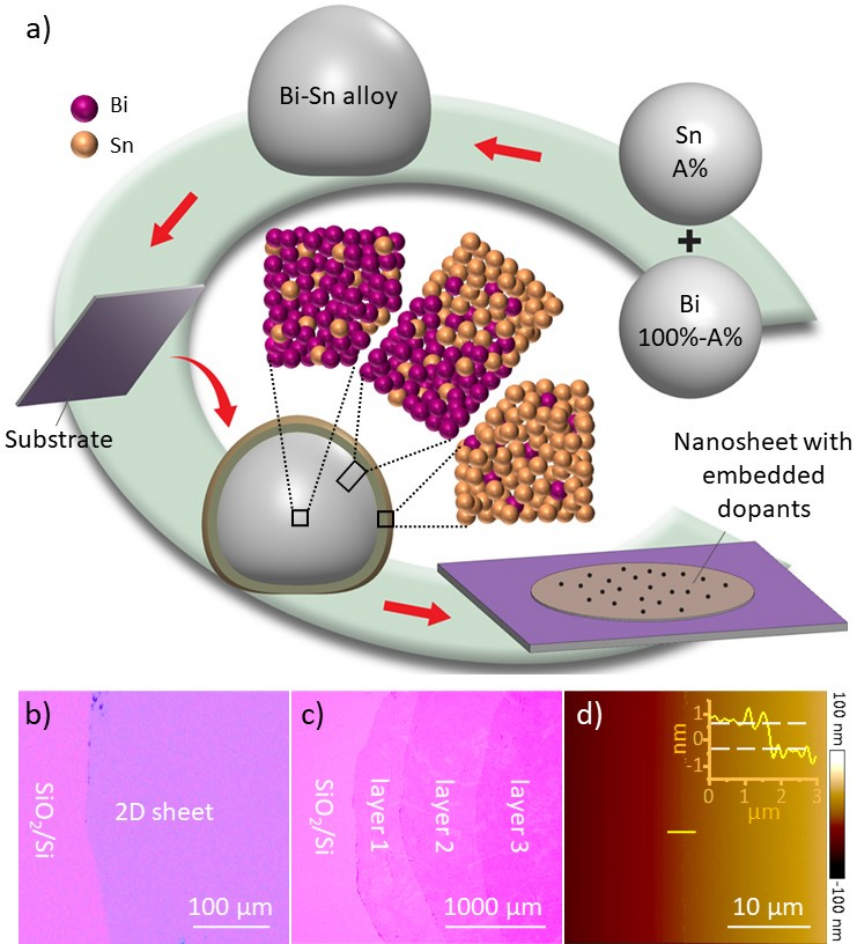

Figure 1. a) Schematic illustration of forming a liquid metal droplet and van der Waals touch printing of 2D sheets from the Bi-Sn liquid metals onto a SiO_2/Si substrate. Sn atoms with

stronger tendency than Bi atoms migrate from the core of the liquid metal to occupy the surface. b,c) The optical images of typical single touch and multi-touch printed oxide nanosheets on SiO_2/Si substrates, respectively. d) AFM topography and height profile of the single-layer oxide material harvested from the surface of 90%Bi liquid metal.

Since the liquid metal is non-polar, there is no covalent bond between the bulk liquid metal and its surface oxide layer. Conversely, the van der Waals interactions between the transfer substrate and surface oxide comprise stronger forces due to the presence of permanent dipoles. Therefore, an atomically thin oxide layer is transferred from the surface of the liquid metal to the substrate when the liquid metal is touched by it.[27, 28]

Large lateral dimensions (i.e. hundreds of microns) and uniform monolayers were obtained from the touch printing process (**Figure 1b**, shows an example of a transfer onto SiO_2/Si substrates). Metallic inclusions could rarely be seen on the nanosheets. Therefore, multiple touch print cycles could be performed in order to controllably increase the number of layers when needed. For instance, **Figure 1c** shows three subsequent touch prints of typical monolayers on a SiO_2/Si substrate. Atomic force microscopy (AFM) was employed to explore the thickness and surface morphology of the layers. As shown in **Figure 1d**, an overall step height of ~1 nm was observed between the oxide nanosheet and the Si substrate. Thicker parts were occasionally produced along the edges of nanosheets (**Figure S1**) due to the restacking and folding of the monolayers during the touch print exfoliation process.

X-ray photoelectron spectroscopy (XPS) was carried out for quantitative measurement of the elemental atomic ratios, as well as the qualitative analysis of their chemical states, in the 2D sheets (**Figure 2a-d**). As a representative demonstration, XPS peak positions for the Sn3*d*, Bi4*f* and O1*s* features for the nanosheet harvested from the surface of 90%Bi liquid alloy are presented in **Figure 2a-c**, respectively. The Sn3d_5 and Sn3d_3 XPS peaks are located at ~486.5 and ~495.3 eV as the characteristic peaks for SnO, which confirms the presence of stannous oxide. Furthermore, no elemental tin was detected due to the absence of peaks at 492.8 and 484.4 eV corresponding to metallic Sn.[25] For the same oxide nanosheet, five distinct peaks appeared in the XPS spectrum of Bi in **Figure 2b**. Peak located at 154.3 eV belonged to the Si2*s* of the substrate while peaks centered at 159.3 and 164.5 eV are assigned to the Bi4f_7 and Bi4f_5 of Bi_2O_3.[29] The changes of the XPS spectra for nanosheets harvested from the surface of 20%Bi, 40%Bi, 57%Bi and 80%Bi alloys with reference to 90%Bi are presented in the insets of **Figure 2a,b**. As can be seen in the inset to **Figure 2a**, the Sn3d_5 and Sn3d_3 peaks are chemically shifted to lower binding energies, likely due to reduced electron screening, when the concentration of Bi decreases in the bulk as a result of reduced Bi incorporation in the harvested layers.[30]

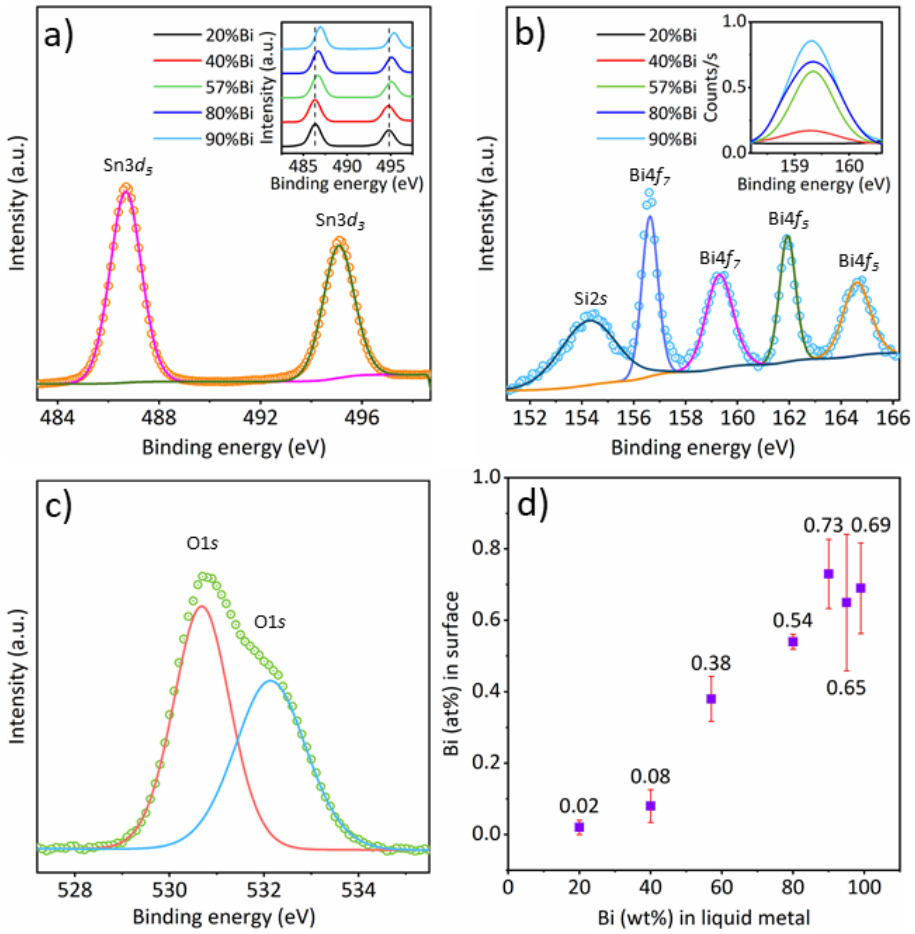

Figure 2. The XPS spectra of a) Sn^{2+} (Sn3d_5 and Sn3d_3), b) Bi^{3+} (Bi4f_7 and Bi4f_5) and c) O^{2-} (O1s) of SiO_2, SnO and Bi_2O_3. Inset in (b) shows the quantitative increase of the Bi_2O_3 Bi4f_7 peak (normalized to Sn3*d* peak intensity) in the oxide layer with the increase of bismuth in the parent alloys. d) Shows the quantitative measurements of Bi^{3+} concentrations (at%) in the oxide layer in contrast to their initial alloy compositions (wt%) obtained from the XPS analysis. Each point and error bar represent

the average composition and standard errors determined for three different measured samples, respectively.

The intensity of the peak at 159.3 eV decreases directly with decreasing ratio of Bi in liquid metal bulk and the reduced incorporation of Bi into the layers (inset in **Figure 2b**). The peaks located at 156.6 and 162 eV (Bi4f_7 & Bi4f_5 respectively) are related to the fractions of elemental bismuth due to the residual Bi metal.[31] It is important to consider that these metallic residue signals are just trace values. The O1*s* spectrum of the nanosheet harvested from the surface of 90%Bi liquid metal was deconvoluted into two major peaks.

The well separated oxygen peak at 532.2 eV is attributed to the SiO_2 substrate and the peak located at 530.4 eV assigned to the lattice oxygen of SnO and Bi_2O_3.[25, 32] These peaks could be similarly observed in all of the other samples. XPS spectra confirmed the dominant oxidation states of Bi^{3+} and Sn^{2+} for Bi and Sn, respectively, ascertaining that the oxide nanosheets are almost devoid of metallic residues.

The atomic ratios obtained from quantitative XPS (**Figure 2d**) were calculated based on the Bi^{3+} and Sn^{2+} ions, while the possible existence of metallic Bi and Sn, and the effect of O^{2-} ions were excluded. The quantitative XPS measurements demonstrated that in stark contrast with the bulk ratios, the Bi content in touch printed interfacial nanosheets was remarkably smaller than the Sn content. The atomic ratios of elemental Bi and Sn in the bulk compared with their detected atomic percentages in the nanosheets are presented in **Figure S2**. By increasing the mass of bismuth in the

bulk from 20 to 90 wt%, the atomic percentages (at%) of Bi^{3+} in the nanosheets increased steadily and ultimately exceeded 0.6 at%, as presented in

Figure 2d. This ratio was effectively stabilized at this point and further accumulation of bismuth in the bulk (even >99%) did not lead to further association of Bi^{3+} in the nanosheets. This observation reveals that Sn is always significantly more dominant within the surface oxide layer even with a significantly lower mass ratio in the bulk. Similar behaviors have also been observed in other 2D materials produced using liquid metal-based synthesis. For example, in a 2D ITO obtained from a liquid metal process, the atomic ratio of Sn in the harvested interfacial layer was much higher than the Sn value in the bulk of the In-Sn alloy.[16] Another example, the non-proportional contribution of elements at the surface of molten alloys was observed where 2D sheets obtained from a eutectic mixture of Te (5 wt%) and Se (95 wt%) resulted in the dominance of TeO_2 (97.7 mol%) in the oxide layer due to the more oxophilic nature of Te relative to Se.[33] Additionally, a recent study [34] predicted the preferential growth of metal oxide layers from binary liquid metal alloys based on some critical factors including the Gibbs free energy of combustion for that alloy, the ratio of metals in the binary alloy and their solubility, and temperature.

Ab initio molecular dynamics simulations were employed to obtain atomic insights into the experimentally observed composition of the Bi_2O_3-doped SnO nanosheets. As shown in **Figure 3a**, in the initial random configuration of 12 Sn in 116 Bi, with six O_2 molecules randomly placed at the interface, only one Sn atom was fully exposed at the interface. At the start of the simulation, the O_2 molecules reacted quickly and spontaneously with the first surface atoms they came in

contact with (predominantly Bi). However, as the simulation progressed, the oxygen atoms migrated through the interface until coming into contact with Sn atoms. At the end of the simulation, all but two O atoms were found to be in direct contact with Sn atoms (**Figure 3b**). Atomic density profiles normal to the interface for the initial (dashed lines) and final (solid lines) configurations are shown in **Figure 3c**. From these results it can be seen that the oxygen penetrates significantly into the interfacial layer, while simultaneously Sn atoms below the interfacial layer migrate towards the interface, to form SnO. Probability distribution functions for the Sn-O and Bi-O pairwise interactions are shown in **Figure 3d**. While the oxygen nearest-neighbor distances are similar for both Bi and Sn, the probability of nearest-neighbor interaction is over five times greater for Sn, despite the fact that it only comprises 10% of the atoms in the layer, and even less at the interface. The nearest neighbor distances for Bi-Bi, Sn-Sn, and Bi-Sn are all nearly identical at ~3.35 Å (**Figure S3**), suggesting that the observed differences are not due to preferential atomic packing arrangements. Altogether, these results demonstrate the migration of Sn to the interface and the preference for SnO formation over Bi_2O_3, even at low Sn concentrations, which explains low concentrations of Bi observed experimentally in the interfacial oxide layer.

The atomic percentage of Bi and Sn materials in the oxide nanosheets might change within certain limitations by varying temperature and oxygen concentration. The passivating oxide layer formation is self-limiting at lower reaction temperatures and 2D materials can no longer be obtained at higher temperatures.[35] Likewise, the oxygen concentration controls the oxidation rate and the thickness of the oxide layer but this does not change the fundamental thermodynamic favorability of

tin oxide over bismuth oxide. Taking these factors into account, changing oxygen concentration and reaction temperature can only vary the bismuth atomic percentage between 0 and ~0.7at%.

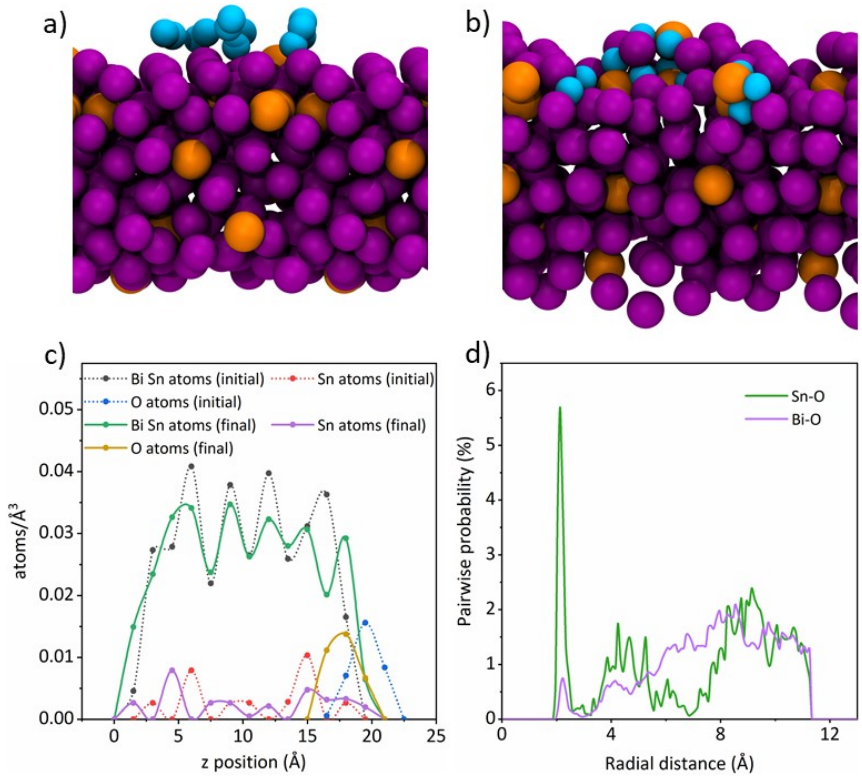

Figure 3. *Ab initio* molecular dynamics simulation snapshots of 12 Sn in 116 Bi, with 6 O_2 molecules on the surface. a) Initial configuration, and b) final configuration. Bi, Sn, and O are colored purple, orange, and blue, respectively. c) Atomic density profiles for Bi, Sn, and O. d) Probability distribution functions for the atom pair distances Sn-O and Bi-O.

Raman spectroscopy was utilized to investigate the presence of bismuth oxide in the tin oxide nanosheets placed on SiO_2/Si substrates (only the oxide nanosheets harvested from the

surface of 90%Bi liquid alloy is presented as the model example, for brevity), as shown in **Figure 4a**. For comparison, SnO and Bi_2O_3 nanosheets were also harvested from metallic tin and bismuth, respectively, as reference samples, and the detailed de-convoluted phonon modes were extracted. The SnO spectrum features the Raman peak at 117 cm^{-1} corresponding to the characteristic E_g modes of SnO.[25] This indicates the absence of other intermediary oxide phases such as Sn_2O_3 and Sn_3O_4. The Raman spectrum of Bi_2O_3 is comprised of several peaks in agreement with the Raman modes of monoclinic α-Bi_2O_3. The A_g mode at 119 cm^{-1} originates from the Bi atoms. A_g and B_g modes at 139 cm^{-1} and 152 cm^{-1}, respectively, are attributed to the displacements of Bi and O atoms in the α-Bi_2O_3 lattice.[36] As shown in **Figure 4a**, nanosheets obtained from the alloy with 90 wt% of Bi exhibit the Raman modes of both SnO and α-Bi_2O_3 at 117, 139 and 152 cm^{-1}, indicating the coexistence of both SnO and α-Bi_2O_3 in the nanosheets.

Figure 4b shows the X-ray diffraction (XRD) patterns of bulk Bi-Sn alloys and oxide nanosheets samples (note the magnified specific peaks from the nanosheets for clarity) with different ratios of Bi and Sn. Touch printing was conducted three separate times to obtain a stronger XRD signal. The XRD patterns of pure Sn and Bi only are also presented at the bottom and top of the figures, respectively, for references. For the bulk XRD patterns, samples containing both elements exhibited the corresponding peaks of Bi and Sn, and by increasing the Bi/Sn ratio in the bulk the intensity of the Bi peak increased proportionally. In the nanosheets counterparts, peaks located at 2θ= ~28° and ~32° correspond to the (120) and (110) planes of Bi_2O_3 and SnO, respectively.[37, 38] However, no Bi_2O_3 peaks in oxide nanosheets are detectable due to the small amount of α-Bi_2O_3 in layers, as confirmed

by XPS measurements. The corresponding XRD peak from the SnO nanosheets at ~32° shifts slightly to the lower diffraction angles when the Bi_2O_3 concentration increases, due to the incorporation of the larger unit cell Bi_2O_3 in the SnO nanosheets.[39] This peak in the nanosheets is hardly visible once the ratio of Bi in bulk increased to ≥80%, due to the creation of a higher concentration of randomly distributed α-Bi_2O_3 structures within the SnO nanosheets. The increased incorporation of α-Bi_2O_3 reduces the possibility of parallel re-stacking of the layers and also enhances the formation of separate SnO clusters. These result in the incoherent refraction of the X-ray signals that lead to the disappearance of the peaks.

For in-depth microscopy analysis, 2D samples were directly deposited on lacey grids for high-resolution transmission electron microscopy (HRTEM). The bright-field TEM image (**Figure 4c**) shows the smooth, ultrathin, and uniform surface of oxide nanosheets harvested from the surface of 90%Bi alloy. A visual comparison between the nanosheets harvested from the surface of 100%Sn sample (SnO) and 90%Bi alloy (SnO doped nanosheets with 0.73 at% of Bi in the form of Bi_2O_3) was provided and the interfaces between SnO and Bi_2O_3 were investigated through the aberration-corrected HRTEM observations and the existence of nano-scale Bi_2O_3 grains were found across SnO nanosheets as shown in **Figure 4d-k.** In the harvested SnO nanosheets, polycrystalline nanograins of SnO were found to be distributed with random orientations and interfaces throughout the nanosheet, as depicted in **Figure 4d**. HRTEM image and the corresponding fast Fourier transform (FFT) image of a SnO nanograin with the lattice spacing of 0.31 nm matching the (011) plane of SnO are shown in **Figure 4e**,**f**, respectively. **Figure 4g** shows the interface of SnO and Bi_2O_3 nanograins

with the dominance of SnO in the nanosheets harvested from the surface of 90%Bi liquid alloy. Here SnO and Bi_2O_3 phases show the *d*-spacing of 0.27 and 0.35 nm, which can be indexed to the $(1\bar{1}0)$ plane of SnO and (002) plane of Bi_2O_3, respectively.[25, 40, 41] The magnified interface of SnO and Bi_2O_3 regions in the doped SnO nanosheets and corresponding FFT pattern are shown in **Figure 4j**,**k**, respectively, indicating the coexistence of SnO and Bi_2O_3 phases in the harvested nanosheets which further confirms the effective doping of SnO nanosheets with Bi_2O_3.

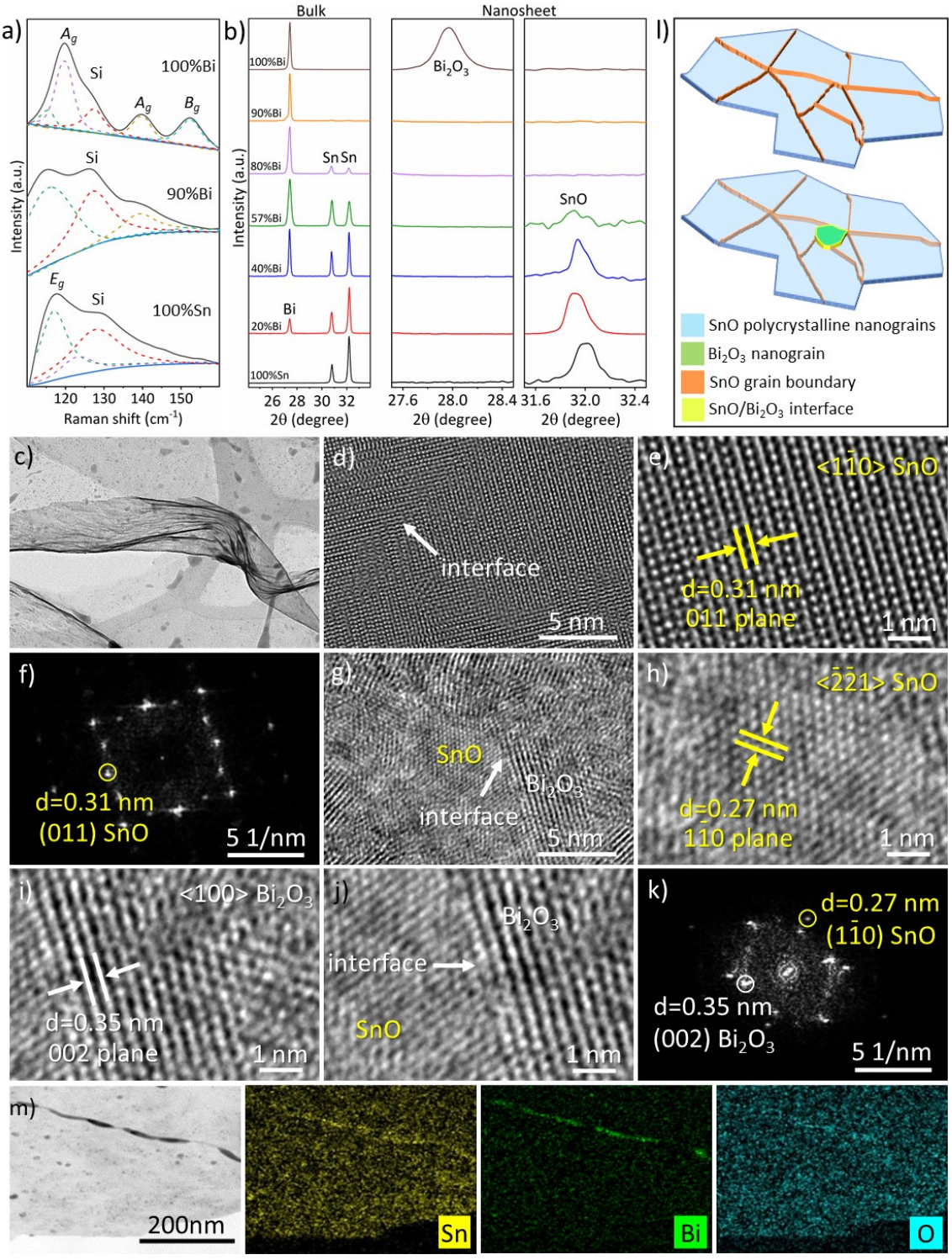

Figure 4. a) The Raman spectra of harvested nanosheets from the surface of 100%Sn, 90%Bi and 100%Bi liquid metals and their individual de-convoluted Raman modes (dash lines), indicating the coexistence of SnO and α-Bi_2O_3 in the nanosheets exfoliated from the surface of 90%Bi liquid metal. Peak located around 130 cm^{-1} is related to the silicon substrate. b) XRD patterns of bulk alloys (left) with different ratios of tin and bismuth, and their corresponding oxide nanosheets (right). c) The bright-field TEM image of nanosheets harvested from the surface of 90%Bi liquid alloy. d) HRTEM image of a SnO nanosheet with observed nanograins and interfaces. e,f) HRTEM image and FFT pattern of a SnO nanograin along the <1-10> direction. g) HRTEM image of Bi_2O_3-doped SnO nanosheet harvested from the surface of 90%Bi liquid metal presenting SnO and Bi_2O_3 phases and their interfaces. h,i) HRTEM images of SnO and Bi_2O_3 nanograins along <-2-21> and <100> directions, respectively. j,k) HRTEM image and corresponding FFT pattern at the interface of SnO and Bi_2O_3 nanograins, respectively in the doped SnO nanosheets. l) The schematic illustration of polycrystalline SnO nanosheets (top) while Bi_2O_3 dopants were randomly dispersed across the SnO nanograins (bottom). m) The EDS mapping of Sn, Bi, O and C elements along to a Bi_2O_3-doped SnO nanosheet harvested from the 90%Bi liquid metal.

The polycrystalline nature of SnO nanosheets both before and after doping with Bi_2O_3 and their interfaces with grain boundaries, based on the aberration-corrected HRTEM observations, are schematically presented in **Figure 4l**. Energy-dispersive X-ray spectroscopy (EDS) elemental mapping shown in **Figure 4k,** displays the distribution of elements across the nanosheets harvested from the

surface of 90%Bi liquid alloy, highlighting the abundance of Sn in comparison to Bi. The EDS elemental mappings of a folded Bi_2O_3-doped SnO nanosheet with large wrinkles are shown in **Figure S4** where Sn and Bi are accumulated within wrinkles and thicker areas, respectively.

For further confirmation of the effect of SnO nanosheets doping, high-resolution atomic force microscopy (HRAFM) was also used for studying the crystallographic properties of nanosheets and exploring the interfaces of Bi_2O_3 grains within doped SnO nanosheets (**Figure S.5**). The spacing identifications for Bi_2O_3 doped SnO crystals (harvested from the surface of 90%Bi liquid metal sample) well matched with crystal structure spacings of SnO and Bi_2O_3.

Electron energy loss spectroscopy (EELS) was employed to determine the band gap (E_g) of the Bi_2O_3-doped SnO nanosheets. EELS is useful for assessing wide band gap materials due to the presence of the zero-peak loss at 0 eV.[27] The enlarged EELS spectra are shown in **Figure 5a** using which the electronic band gaps of the nanosheets were determined by extrapolating the linear fits of the electron loss energy to loss intensity. The nanosheets exfoliated from the surface of 100%Sn and 100%Bi liquid metals indicated band gaps of 4.2 and 3.5 eV, respectively, in agreement with previously reported band gaps for monolayers of SnO [25] and α-Bi_2O_3.[32] As shown in the inset to **Figure 5a**, the band gap of SnO nanosheets firstly plunges to 2.7eV by the inclusion of only 0.02 at% of Bi_2O_3 in the sheets, followed by a continuous increase to around 3 eV for the Bi_2O_3-doped SnO nanosheet harvested from the surface of 90%Bi liquid metal (0.73 at% at the surface) which is closer to the band gap of 2D α-Bi_2O_3. Similar variations in the band gap of SnO have been reported with the additional ratios of La [42] and Cr [43] dopants. The narrowing of the band gap may arise from different

interaction effects among free charge carriers or between free carriers and ionized impurities [44] and can be interpreted by *sp-d* exchange interactions.[45] For SnO, the orbital electrons of Sn 5*s* and O 2*p* mainly form the valence band including the highest occupied state, the valence band maximum (VBM), while conduction band contains the Sn 5*p* electron states, to the conduction band minimum (CBM).[43] In the case of low Bi concentrations, the doping ions dominantly move into the Bi substituted lattice sites of Sn (Bi_{Sn}). Localized *d*- orbital electrons of Bi_{Sn} can interact with both *s*- and *p*-orbital electrons, which leads to negative and positive modulation of the CBM and VBM edges, respectively, and causing the observed band gap contraction effect.[43] On the other hand, an observed increase in the measured band gap can be explained based on the well-known Burstein-Moss effect,[46] when the Fermi level moves higher in to the conduction band due to the increase in carrier concentration, hence low-energy transitions are blocked, and band gap increases.[47]

A non-linear least squares equation solver in the MATLAB optimization toolbox was used for fitting and interpreting the nature of the measured band gaps using $\alpha h\nu \propto (h\nu - E_g)^n$, where $h\nu$ is the photon energy and α is a constant. Here, n = 2 and 1/2 correspond to the indirect and direct transitions, respectively.[27] As shown in **Figure S6**, both the SnO (4.2 eV) and Bi_2O_3 (3.6 eV) nanosheets present excellent fits to indirect and direct band gaps, respectively, which are in agreement with earlier reports.[25, 32] The Bi_2O_3-doped SnO nanosheets harvested from surface of 90%Bi (3.1 eV) alloy which is predominantly composed of SnO also possessed an indirect band gap.

Electronic work functions, which indicate the energy difference between vacuum level and the Fermi level, were acquired through a linear fit to the secondary electron cut-off in ultraviolet

photoelectron spectroscopy (UPS) spectra of oxide nanosheets as shown in **Figure 5b**. Since the work function is a surface property, it is strongly affected by variation in surface structure and composition.[48] Work functions of 4.7 eV and 3.8 eV were found for SnO and Bi_2O_3, respectively, in agreement with the literature.[49-51] As reflected in **Figure 5b**, immediately after minor doping of the SnO nanosheets with Bi_2O_3 (0.02 at% of Bi at 20%Bi sample), the work function dropped by 0.4 eV (8.5%) followed by a steady decrease from SnO (4.7 eV) to Bi_2O_3 (3.8 eV). VBM values were determined through the interception of the XPS valence band spectra from the oxide nanosheets. As shown in **Figure 5c** and the corresponding inset graph, the Fermi level-VBM separation increased gradually in oxide nanosheets from 1.4 to 2.9 eV by increasing the atomic ratio of Bi from 0% to 100% in the bulk. The position of CBM was obtained from the $E_g = E_{VB} - E_{CB}$ equations and are listed together with E_g and VBM values in **Table 1**. In order to verify the results obtained by EELS and UPS, Mott–Schottky measurements were used within the electrolyte environment. This was done to determine the flat band potentials (E_{fb}) for the Bi_2O_3-doped SnO nanosheets as the estimation of their conduction band or valence band potentials and the carrier type of these semiconductor materials.

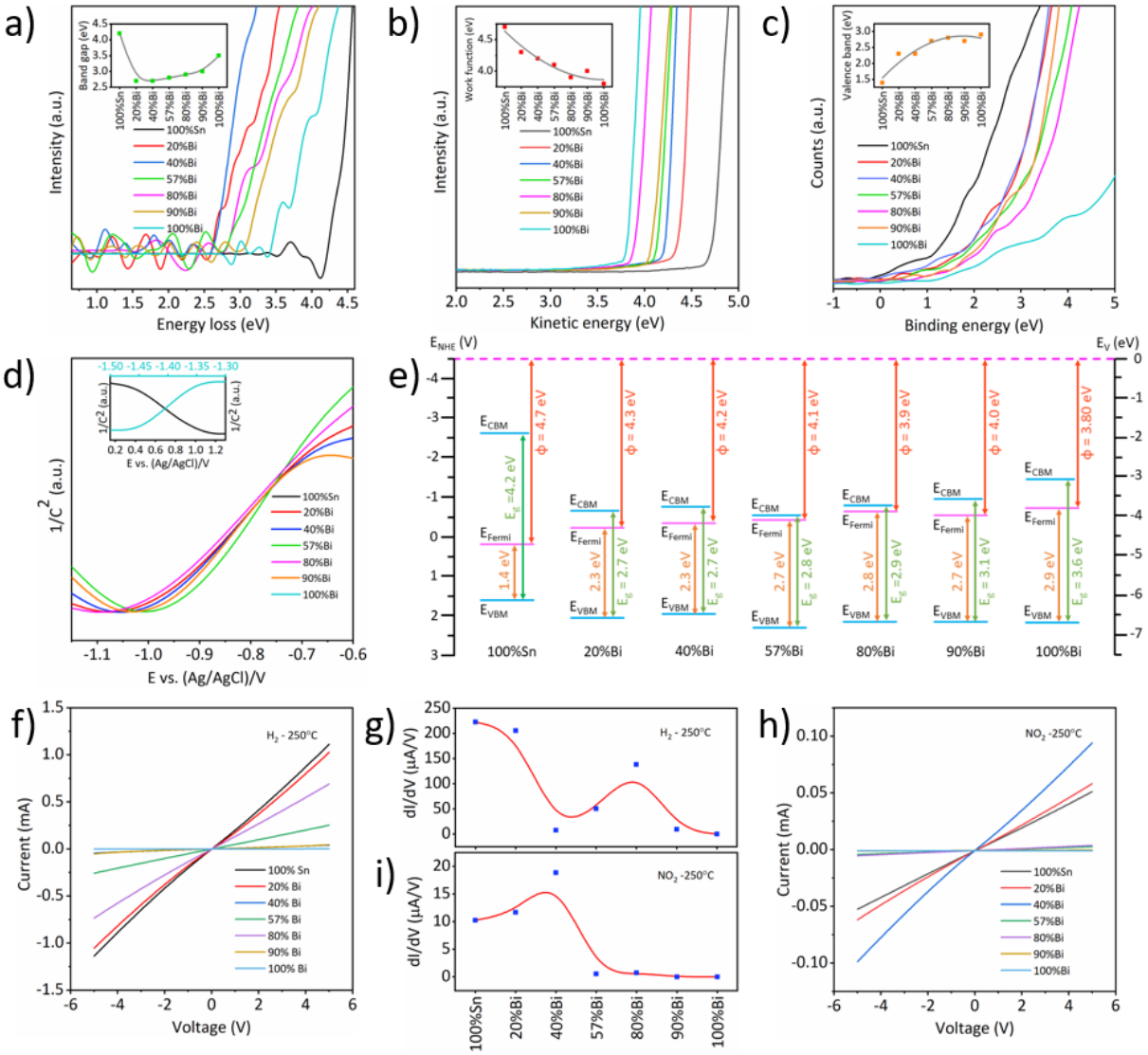

Figure 5. a) EELS spectra as the estimation of band gaps, b) UPS spectra as the estimation of work functions and c) XPS valence bands of the touch-printed Bi_2O_3-doped SnO 2D materials. Insets in (a-c) indicate the trend of changes in band gaps, work functions and valence bands, respectively, with increasing the atomic ratio of Bi in samples. d) Mott-Schottky plots of n-type oxide nanosheets with

different ratios of Bi. Inset shows the Mott-Schottky plots of the p-type SnO and n-type Bi_2O_3 nanosheets. e) The band structures of Bi_2O_3-doped SnO 2D materials obtained from EELS, UPS and XPS measurements shown in (a-c). I-V characteristic graphs and conductivity variations (dI/dV) of oxide nanosheets with different atomic ratios of Bi measured at 250°C in f,g) H_2 and h,i) NO_2 gas atmospheres.

Table 1. Values for the electronic structure of Bi_2O_3, Bi_2O_3-doped SnO and SnO nanosheets (harvested from the surface of 100%Sn, 20%Bi, 20%Bi, 40%Bi, 57%Bi, 80%Bi, 90%Bi and 100%Bi liquid metal samples) obtained using EELS, UPS secondary electron cut-off, XPS valence band and Mott–Schottky measurements.

Sample	Band gap (E_g)	Work function (ϕ)	Flat band potential (E_{fb})	Valence band (eV)	Valence band maximum (VBM)			Conduction band minimum (CBM)		
					a	b	c	a	b	c
100%Sn	4.2	4.7	1.10	1.4	-6.1	-5.78	1.30	-1.9	-	-
20%Bi	2.7	4.3	-1.00	2.3	-6.6	-	-	-3.9	-3.68	-0.80

40%Bi	2.7	4.2	-0.98	2.3	-6.5	-	-	-3.8	-3.70	-0.78
57%Bi	2.8	4.1	-0.94	2.7	-6.8	-	-	-4.0	-3.74	-0.74
80%Bi	2.9	3.9	-1.10	2.8	-6.7	-	-	-3.8	-3.58	-0.90
90%Bi	3.1	4.0	-0.96	2.7	-6.7	-	-	-3.7	-3.72	-0.76
100%Bi	3.6	3.8	-1.45	2.9	-6.7	-	-	-3.2	-3.22	-1.25

[a] acquired using XPS and UPS measurements

[b] acquired through Mott–Schottky measurements versus vacuum

[c] acquired through Mott–Schottky measurements versus NHE

Generally, Mott–Schottky plots with positive and negative slopes indicate the typical n-type and p-type semiconductor behaviour, respectively. In addition, the flat band potential in n-type semiconductors is close to the CBM, while the flat band potential is close to the VBM in p-type semiconductors.[52] The Mott-Schottky plots of oxide nanosheets are shown in **Figure 5d** indicating the p-type nature of SnO and the n-type characteristic of Bi_2O_3-doped SnO nanosheets. Flat band

potentials of 1.10 V and -1.45 V versus Ag/AgCl were obtained from the onset of the Mott–Schottky plots for SnO and Bi_2O_3 nanosheets respectively, as shown in the inset of **Figure 5d.** The E_{VB} and E_{CB} versus normal hydrogen electrode (NHE) is calculated through $E_{CB,VB} = E_{Ag/AgCl} + E_{fb}$ equation where $E_{Ag/AgCl}$ is 0.197 V.[53] On the other side, the E_{VB} and E_{CB} versus vacuum also can be calculated through $E_{CB,VB} = E_{Ag/AgCl} - E_{fb}$ equation where $E_{Ag/AgCl}$ is −4.675 V.[54] Consequently, the E_{VB} versus NHE and vacuum were estimated as 1.30 V and -5.78 eV for SnO nanosheets and E_{CB} versus NHE and vacuum were estimated as -1.25 V and -3.22 eV for Bi_2O_3 nanosheets, respectively. The E_{CB} of the other n-type Bi_2O_3-doped SnO nanosheets were listed in **Table 1** which are in agreement with earlier results however the slight difference in the band positions might be related to the alkaline pH environments in the Mott–Schottky measurements.

The electronic band structures of the 2D Bi_2O_3, Bi_2O_3-doped SnO and SnO nanosheets with varying ratios of Sn and Bi were established through the XPS, UPS and EELS measurements that are shown in **Figure 5e** and the data can be found in **Table 1**. Also, the extended EELS, UPS and valence band spectra of oxide nanosheets are shown in **Figure S7**.

In order to explore a typical application of this novel semiconductor doping method, a series of electronic transducers were developed, and their responses were analyzed when exposed to both reducing and oxidizing gases. Here Au/Cr electrodes were deposited onto the Sn nanosheets of different Bi_2O_3 dopant ratios (**Figure S8**). As references, Bi_2O_3 and SnO sheets were also compared. Then current versus voltage (I-V) curves of the nanosheets in response to H_2 exposure (reducing gas – 2.02% in synthetic air) and NO_2 (oxidizing gas - 9 ppm in synthetic air) as gases, in zero air

background, between -5V and 5V at 250°C were recorded. It is known that SnO is a sensitive material for gas sensing.[55-57] As can be seen in **Figure 5f,g**, SnO and Bi_2O_3 presented the lowest and highest resistance, respectively, and the current dropped consistently from 1 mA to 1 µA by increasing the Bi ratio in the bulk liquid metal. This can be considered as an indication of the emergence of Bi_2O_3 dopant in the SnO nanosheets. The frequent distribution of n-type Bi_2O_3 across the p-type SnO might cause the depletion of charge carriers and subsequently increase the resistance.[58] Among the samples, Bi_2O_3-doped SnO harvested from the surface of 40%Bi liquid metal alloy (0.08 at% Bi in the nanosheets) possessed the lowest conductivity which was close to that of Bi_2O_3. The magnified view of the I-V curve for oxide nanosheets collected from the surface of 100%Bi liquid metal in **Figure S9** shows the non-linear nature of I-V curves generated during the measurements in the reducing H_2 environment, indicating Schottky-type electron transportation.

The same set of measurements were carried out for nanosheets in the presence of NO_2 gas at 250°C to monitor the corresponding I-V curves, as shown in **Figure 5h,i**. Similar to the H_2 environments, SnO nanosheets recorded a lower resistance compared to Bi_2O_3, however, the resistance was higher than Bi_2O_3-doped SnO nanosheets harvested from the surface of 20%Bi alloy (0.02 at% Bi in nanosheet) and almost twice as high as the 40% Bi alloy (0.08 at% Bi in nanosheet) nanosheets in the NO_2 atmosphere (**Figure 5i**). Opposite to the response to the H_2 gas, the nanosheets exfoliated from the surface of 40%Bi liquid metal exhibited the highest conductivity when exposed to NO_2. The enhanced sensitivity of the fabricated Bi_2O_3-doped SnO nanosheets in presence of NO_2 might be attributed to the n-type Bi_2O_3 doping.[59] As a result a hole-depletion region in p-type SnO and an

electron-depletion region in n-type Bi_2O_3 are produced at the interface of SnO and Bi_2O_3 due to energy band bending. Since SnO is the dominant phase in the touch-printed nanosheets, a high resistance is expected in air due to the narrowed hole-accumulation in SnO caused by the depletion region. However, when the Bi_2O_3-doped SnO nanosheets are exposed to NO_2 gas, holes are generated which leads to the decrease of the barrier height at the p-n boundaries, expansion of the hole accumulation layer and a widening of the conduction channel in SnO. Therefore, the conductivity of the oxide nanosheets increases significantly and a high response value can be expected from the Bi_2O_3-doped SnO nanosheets. The maximum and minimum conductivity for the Bi_2O_3-doped SnO nanosheets harvested from the 40%Bi alloy (0.08 at% Bi in nanosheet) in NO_2 and H_2 gases, respectively, shows the optimized composition and offers the possible application of selective sensing of H_2 and NO_2.[60] This example shows the potential merit of this work as to how easily and with no expensive equipment and only by relying on the selective enrichment of the Bi-Sn alloy, dopant concentration could be controlled for a very specific application.

3. Conclusions

The ability of liquid metals to selectively filter elements to their interfaces has been used for harvesting SnO nanosheets doped with Bi_2O_3. The surface of the liquid Bi-Sn alloys showed

a dramatically different nature and stoichiometry compared to the bulk structure. Despite the considerable increase in the fraction of Bi compared to Sn in the bulk, the atomic percentage of Bi within the surface layer of the Bi-Sn alloys increased at a much smaller rate, and only recorded a maximum level of ~0.7 at% when the Bi ratios were as high as 90% in the bulk. The molecular dynamics simulations explained the higher tendency of Sn rather than Bi to migrate to the surface of the liquid metal, and the preference of O to interact with Sn rather than Bi, in agreement with the experimental and quantitative measurements. This unique ability introduces a new pathway for the controllable and selective doping of 2D materials. The Bi_2O_3-doped SnO nanosheets obtained consistently showed n-type behaviour, despite the p-type nature of SnO. The SnO nanosheets, with varying amounts of Bi_2O_3 dopants, were examined for their ability at sensing both H_2 and NO_2 gases. While the doping method illustrates how the harvested materials could become selective to NO_2 simply by modulating the bulk concentration that affects the trace amounts of surface doping. The controlled doping method presented in this paper heralds a new process for monitoring the interfacially migrated dopants using the natural filtering properties of liquid metal based alloys. This work has huge potential to impact several processes in the fabrication of metal oxide semiconductor devices for large scale applications.

4. Experimental Section/Methods

Materials: Sn (99.9%) and Bi (99.99%) were purchased from Rotometals, USA.

Characterization: The topography and thickness of the nanosheets were assessed by AFM on a Bruker Dimension ICON SPM while the HRAFM images were obtained by a Cypher ES Atomic Force Microscope (Oxford Instrument, Asylum Research) using amplitude modulated-AFM. XPS and valence band analysis were performed on conductive substrates using a Thermo Scientific K-alpha XPS spectrometer equipped with a monochromatic Al K_α source (*hv* = 1486.6 eV) and a concentric hemispherical electron analyser (CHA). The pass energy of the analyser was set to 30 eV for the reported core-level spectra and 100 eV for the wider survey scans (not shown). The work functions of the samples were acquired through UPS measurements of the secondary electron cut-off using the He (I) emission line (*hv* = 21.2 eV) from a helium gas-discharge lamp and the CHA.

The phase composition of the bulk and 2D materials were investigated using a multi-purpose XRD and an Empyrean thin-film XRD instrument, respectively (both using Cu K_α radiation with λ=1.54 Å). The morphology of nanosheets was captured by JEOL F200 TEM, with EDS for the chemical compositions. Aberration-corrected HRTEM images were captured using a Titan Themis-Z double-corrected microscope operated at 300 kV. The phase of the touch printed nanosheets, and their deformation as a function of the bismuth ratio were observed through Raman spectroscopy (inVia Renishaw). The band-gaps of the nanosheets were determined using a JEOL 2100F EELS at 200 kV equipped with a Gatan Tridium imaging filter and the acquired data were fitted into energy equations in MATLAB curve fitting toolbox. Mott–Schottky measurements were obtained through a standard three electrode set-up and CHI650E electrochemical workstation (CHI Instrument Co.) to further examine the band structures. The cell set-up included an Ag/AgCl (in 3M NaCl)

reference electrode, an Au counter electrode and a working electrode that was 1×1 cm silicon wafer coated with Bi_2O_3-doped SnO nanosheets. The electrolyte (0.3 mol L^{-1} Na_2SO_4) was degassed by purging nitrogen. Series of Au/Cr electrodes with a total size of 2 mm and electrode gap of 25 µm were deposited on oxide nanosheets using an e-beam evaporator deposition system (HHV, ATS500) for device fabrication and I-V curve measurements in H_2 (2.02% H_2 balanced in synthetic air) and NO_2 (9.0 ppm NO_2 balanced in synthetic air) atmospheres. The device I-V characteristics were measured using a precision source and measurement unit (Keysight B2912A).

Molecular dynamics simulations: *Ab initio* molecular dynamics simulations were performed to obtain atomic insights into the experimentally observed composition of the oxide layers. In order to generate initial random configurations of 12 Sn atoms in 116 Bi (~10 at% Sn) in a 15.9 × 15.9 × 15.9 $Å^3$ box, classical MD simulations using the MD code LAMMPS were performed.[61] Sigma and epsilon values for Sn were 2.82 Å and 1.65 kcal mol^{-1}, respectively, and for Bi 3.04 Å and 1.78 kcal mol^{-1}, respectively. A 15 Å vacuum spacer was added in the z dimension to the equilibrated system, and 6 O_2 molecules were added at ~3 Å from the surface. *Ab initio* molecular dynamics simulations were subsequently carried out in the Vienna *ab initio* Simulation Package (VASP) [62, 63] at 623 K with the Perdew–Burke–Ernzerhof (PBE) exchange correlation functional, a 3 × 3 × 1 k-point grid, and an energy cutoff of 500 eV.

Supporting Information

Supporting Information is available from the Wiley Online Library or from the author.

Acknowledgements

The authors would like to acknowledge the Australian Research Council (ARC) Laureate Fellowship grant (FL180100053) and ARC Center of Excellence FLEET (CE170100039) for the financial coverage of this work. The authors also acknowledge the facilities and the scientific and technical assistance of Microscopy Australia at the Electron Microscope Unit (EMU) within the Mark Wainwright Analytical Centre (MWAC) at UNSW Sydney, and Sydney Microscopy & Microanalysis, the University of Sydney node of Microscopy Australia. This research was undertaken with the assistance of supercomputing resources from the National Computational Infrastructure (NCI), which is supported by the Australian Government, under the National Computational Merit Allocation Scheme (project kl59).

Received: ((will be filled in by the editorial staff))
Revised: ((will be filled in by the editorial staff))
Published online: ((will be filled in by the editorial staff))

References

[1] J. Li, X. Zhang, B. Yang, C. Zhang, T. Xu, L. Chen, L. Yang, X. Jin, B. Liu, *Chem. Mater.* **2021**.

[2] M. B. Ghasemian, M. Mayyas, S. A. Idrus-Saidi, M. A. Jamal, J. Yang, S. S. Mofarah, E. Adabifiroozjaei, J. Tang, N. Syed, A. P. O'Mullane, T. Daeneke, K. Kalantar-Zadeh, *Adv. Funct. Mater.* **2019**, *29*, 1901649.

[3] W. Hu, Y. Li, S.-Y. Tang, L. Li, Q. J. Niu, S. Yan, *Adv. Mater. Interfaces* **2021**, *8*, 2170058.

[4] Y. Wang, S. Wang, H. Chang, W. Rao, *Adv. Mater. Interfaces* **2020**, *7*, 2000626.

[5] L. Ren, N. Cheng, X. Man, D. Qi, Y. Liu, G. Xu, D. Cui, N. Liu, J. Zhong, G. Peleckis, X. Xu, S. X. Dou, Y. Du, *Adv. Mater. Interfaces* **2021**, *33*, 2008024.

[6] J.-H. Fu, T.-Y. Liu, Y. Cui, J. Liu, *Adv. Mater. Interfaces* **2021**, *8*, 2001936.

[7] S. Chen, H.-Z. Wang, R.-Q. Zhao, W. Rao, J. Liu, *Matter* **2020**, *2*, 1446.

[8] E. Wang, J. Shu, H. Jin, Z. Tao, J. Xie, S.-Y. Tang, X. Li, W. Li, M. D. Dickey, S. Zhang, *iScience* **2021**, *24*, 101911.

[9] S. Zhao, J. Zhang, L. Fu, *Adv. Mater.* **2021**, *33*, 2005544.

[10] Y. Ding, X. Guo, Y. Qian, L. Xue, A. Dolocan, G. Yu, *Adv. Mater.* **2020**, *32*, 2002577.

[11] Y. Liu, W. Zhang, H. Wang, *Mater. Horiz.* **2021**, *8*, 56.

[12] E. P. Nguyen, T. Daeneke, S. Zhuiykov, K. Kalantar-Zadeh, *Curr. Protoc. Chem. Biol.* **2016**, *8*, 97.

[13] M. Karbalaei Akbari, F. Verpoort, S. Zhuiykov, *J. Mater. Chem. A* **2021**, *9*, 34.

[14] A. Zavabeti, J. Z. Ou, B. J. Carey, N. Syed, R. Orrell-Trigg, E. L. H. Mayes, C. Xu, O. Kavehei, A. P. O'Mullane, R. B. Kaner, K. Kalantar-zadeh, T. Daeneke, *Science* **2017**, *358*, 332.

[15] J. Tang, S. Lambie, N. Meftahi, A. J. Christofferson, J. Yang, M. B. Ghasemian, J. Han, F.-M. Allioux, M. A. Rahim, M. Mayyas, T. Daeneke, C. F. McConville, K. G. Steenbergen, R. B. Kaner, S. P. Russo, N. Gaston, K. Kalantar-Zadeh, *Nat. Nanotechnol.* **2021**, *16*, 431.

[16] R. S. Datta, N. Syed, A. Zavabeti, A. Jannat, M. Mohiuddin, M. Rokunuzzaman, B. Yue Zhang, M. A. Rahman, P. Atkin, K. A. Messalea, M. B. Ghasemian, E. D. Gaspera, S. Bhattacharyya, M. S. Fuhrer, S. P. Russo, C. F. McConville, D. Esrafilzadeh, K. Kalantar-Zadeh, T. Daeneke, *Nat. Electron.* **2020**, *3*, 51.

[17] M. B. Ghasemian, T. Daeneke, Z. Shahrbabaki, J. Yang, K. Kalantar-Zadeh, *Nanoscale* **2020**, *12*, 2875.

[18] W. Yang, J. Li, X. Zhang, C. Zhang, X. Jiang, B. Liu, *Inorg. Chem.* **2019**, *58*, 549.

[19] C. Liu, B. Wang, G. Jia, P. Liu, H. Yin, S. Guan, Z. Cheng, *Appl. Phys. Lett.* **2021**, *118*, 072902.

[20] R. Chen, F. Luo, Y. Liu, Y. Song, Y. Dong, S. Wu, J. Cao, F. Yang, A. N'Diaye, P. Shafer, Y. Liu, S. Lou, J. Huang, X. Chen, Z. Fang, Q. Wang, D. Jin, R. Cheng, H. Yuan, R. J. Birgeneau, J. Yao, *Nat. Commun.* **2021**, *12*, 3952.

[21] K. Kang, S. Fu, K. Shayan, Y. Anthony, S. Dadras, X. Yuzan, F. Kazunori, M. Terrones, W. Zhang, S. Strauf, V. Meunier, A. N. Vamivakas, E.-H. Yang, *Nanotechnology* **2020**, *32*, 095708.

[22] N. R. Glavin, R. Rao, V. Varshney, E. Bianco, A. Apte, A. Roy, E. Ringe, P. M. Ajayan, *Adv. Mater.* **2020**, *32*, 1904302.

[23] A. Chaves, J. G. Azadani, H. Alsalman, D. R. da Costa, R. Frisenda, A. J. Chaves, S. H. Song, Y. D. Kim, D. He, J. Zhou, A. Castellanos-Gomez, F. M. Peeters, Z. Liu, C. L. Hinkle, S.-H. Oh, P. D. Ye, S. J. Koester, Y. H. Lee, P. Avouris, X. Wang, T. Low, *NPJ 2D Mater. Appl.* **2020**, *4*, 29.

[24] N. E. Quackenbush, J. P. Allen, D. O. Scanlon, S. Sallis, J. A. Hewlett, A. S. Nandur, B. Chen, K. E. Smith, C. Weiland, D. A. Fischer, J. C. Woicik, B. E. White, G. W. Watson, L. F. J. Piper, *Chem. Mater.* **2013**, *25*, 3114.

[25] T. Daeneke, P. Atkin, R. Orrell-Trigg, A. Zavabeti, T. Ahmed, S. Walia, M. Liu, Y. Tachibana, M. Javaid, A. D. Greentree, S. P. Russo, R. B. Kaner, K. Kalantar-Zadeh, *ACS Nano* **2017**, *11*, 10974.

[26] J. Tang, R. Daiyan, M. B. Ghasemian, S. A. Idrus-Saidi, A. Zavabeti, T. Daeneke, J. Yang, P. Koshy, S. Cheong, R. D. Tilley, R. B. Kaner, R. Amal, K. Kalantar-Zadeh, *Nat. Commun.* **2019**, *10*, 4645.

[27] M. B. Ghasemian, A. Zavabeti, R. Abbasi, P. V. Kumar, N. Syed, Y. Yao, J. Tang, Y. Wang, A. Elbourne, J. Han, M. Mousavi, T. Daeneke, K. Kalantar-Zadeh, *J. Mater. Chem. A* **2020**, *8*, 19434.

[28] N. Mahmood, H. Khan, K. Tran, P. Kuppe, A. Zavabeti, P. Atkin, M. B. Ghasemian, J. Yang, C. Xu, S. A. Tawfik, M. J. S. Spencer, J. Z. Ou, K. Khoshmanesh, C. F. McConville, Y. Li, K. Kalantar-Zadeh, *Mater. Today* **2021**, *44*, 69.

[29] I. Fujita, P. Edalati, Q. Wang, M. Watanabe, M. Arita, S. Munetoh, T. Ishihara, K. Edalati, *Scr. Mater.* **2020**, *187*, 366.

[30] X. Kou, F. Meng, K. Chen, T. Wang, P. Sun, F. Liu, X. Yan, Y. Sun, F. Liu, K. Shimanoe, G. Lu, *Sens. Actuators, B* **2020**, *320*, 128292.

[31] M. Mousavi, M. B. Ghasemian, J. Han, Y. Wang, R. Abbasi, J. Yang, J. Tang, S. A. Idrus-Saidi, X. Guan, M. J. Christoe, S. Merhebi, C. Zhang, J. Tang, R. Jalili, T. Daeneke, T. Wu, K. Kalantar-Zadeh, M. Mayyas, *Appl. Mater. Today* **2021**, *22*, 100954.

[32] K. A. Messalea, B. J. Carey, A. Jannat, N. Syed, M. Mohiuddin, B. Y. Zhang, A. Zavabeti, T. Ahmed, N. Mahmood, E. Della Gaspera, K. Khoshmanesh, K. Kalantar-Zadeh, T. Daeneke, *Nanoscale* **2018**, *10*, 15615.

[33] A. Zavabeti, P. Aukarasereenont, H. Tuohey, N. Syed, A. Jannat, A. Elbourne, K. A. Messalea, B. Y. Zhang, B. J. Murdoch, J. G. Partridge, M. Wurdack, D. L. Creedon, J. van Embden, K. Kalantar-Zadeh, S. P. Russo, C. F. McConville, T. Daeneke, *Nat. Electron.* **2021**, *4*, 277.

[34] A. Goff, P. Aukarasereenont, C. K. Nguyen, R. Grant, N. Syed, A. Zavabeti, A. Elbourne, T. Daeneke, *Dalton Trans.* **2021**, *50*, 7513.

[35] N. Cabrera, N. F. Mott, *Rep. Prog. Phys.* **1949**, *12*, 163.

[36] C.-H. Ho, C.-H. Chan, Y.-S. Huang, L.-C. Tien, L.-C. Chao, *Opt. Express* **2013**, *21*, 11965.

[37] T. Tran-Phu, R. Daiyan, Z. Fusco, Z. Ma, R. Amal, A. Tricoli, *Adv. Funct. Mater.* **2020**, *30*, 1906478.

[38] M. Singh, E. D. Gaspera, T. Ahmed, S. Walia, R. Ramanathan, J. van Embden, E. Mayes, V. Bansal, *2d Mater.* **2017**, *4*, 025110.

[39] M. B. Ghasemian, A. Rawal, Y. Liu, D. Wang, *ACS Appl. Mater. Interfaces* **2018**, *10*, 20816.

[40] J. S. Dias, F. R. M. Batista, R. Bacani, E. R. Triboni, *Sci. Rep.* **2020**, *10*, 9446.

[41] T. Selvamani, S. Anandan, L. Granone, D. W. Bahnemann, M. Ashokkumar, *Mater. Chem. Front.* **2018**, *2*, 1664.

[42] S. Yim, T. Kim, B. Yoo, H. Xu, Y. Youn, S. Han, J. K. Jeong, *ACS Appl. Mater. Interfaces* **2019**, *11*, 47025.

[43] G. Dai, W. Zhou, X. Ma, J. Yuan, P. Wu, *Ceram. Int.* **2020**, *46*, 13350.

[44] M. Thirumoorthi, J. T. J. Prakash, *Superlattices Microstruct.* **2016**, *89*, 378.

[45] X. Qiu, L. Li, G. Li, *Appl. Phys. Lett.* **2006**, *88*, 114103.

[46] T. S. Moss, *Proc. Phys. Soc.* **1954**, *67*, 775.

[47] M. Arshad, A. Azam, A. S. Ahmed, S. Mollah, A. H. Naqvi, *J. Alloys Compd.* **2011**, *509*, 8378.

[48] S. Halas, T. Durakiewicz, *Vacuum* **2010**, *85*, 486.

[49] X. Li, L. Liang, H. Cao, R. Qin, H. Zhang, J. Gao, F. Zhuge, *Appl. Phys. Lett.* **2015**, *106*, 132102.

[50] J.-g. Guo, Y. Liu, Y.-j. Hao, Y.-l. Li, X.-j. Wang, R.-h. Liu, F.-t. Li, *Appl. Catal. B* **2018**, *224*, 841.

[51] J. Chen, K. Qiu, *Colloids Surf., A* **2021**, *615*, 126262.

[52] R. Zhang, Q. Wang, J. Zhang, Q. Lu, W. Liu, S. Yin, W. Cao, *Nanotechnology* **2019**, *30*, 434001.

[53] W. Liu, B. Liang, Y. Ma, Y. Liu, A. Zhu, P. Tan, X. Xiong, J. Pan, *J. Colloid Interface Sci.* **2017**, *508*, 559.

[54] S. A. Idrus-Saidi, J. Tang, M. B. Ghasemian, J. Yang, J. Han, N. Syed, T. Daeneke, R. Abbasi, P. Koshy, A. P. O'Mullane, K. Kalantar-Zadeh, *J. Mater. Chem. A* **2019**, *7*, 17876.

[55] P. H. Suman, A. A. Felix, H. L. Tuller, J. A. Varela, M. O. Orlandi, *Sens. Actuators, B* **2013**, *186*, 103.

[56] M. S. Barbosa, P. H. Suman, J. J. Kim, H. L. Tuller, J. A. Varela, M. O. Orlandi, *Sens. Actuators, B* **2017**, *239*, 253.

[57] A. Shanmugasundaram, P. Basak, L. Satyanarayana, S. V. Manorama, *Sens. Actuators, B* **2013**, *185*, 265.

[58] A. P. Dral, J. E. ten Elshof, *Sens. Actuators, B* **2018**, *272*, 369.

[59] L. Li, C. Zhang, W. Chen, *Nanoscale* **2015**, *7*, 12133.

[60] H.-S. Jeong, M.-J. Park, S.-H. Kwon, H.-J. Joo, S.-H. Song, H.-I. Kwon, *Ceram. Int.* **2018**, *44*, 17283.

[61] S. Plimpton, *J. Comput. Phys.* **1995**, *117*, 1.

[62] G. Kresse, J. Furthmüller, *Phys. Rev. B* **1996**, *54*, 11169.

[63] G. Kresse, D. Joubert, *Phys. Rev. B* **1999**, *59*, 1758.

The interface of liquid metals is used as natural filtering for doping and harvesting two-dimensional doped metal oxide semiconductors. 2D Bi_2O_3-doped SnO semiconducting sheets are produced based on the different migration tendencies of Sn and Bi metals within the bulk competing for the selective enrichment of the liquid metal interface.

Mohammad B. Ghasemian,* Ali Zavabeti, Maedehsadat Mousavi, Billy J. Murdoch, Andrew J. Christofferson, Nastaran Meftahi, Jianbo Tang, Jialuo Han, Rouhollah Jalili, Francois-Marie Allioux, Mohannad Mayyas, Zibin Chen, Aaron Elbourne, Chris F. McConville, Salvy P. Russo, Simon Ringer, and Kourosh Kalantar-Zadeh*

Doping Process of Two-Dimensional Materials Based on the Selective Migration of Dopants to the Interface of Liquid Metals

ToC figure